Chen, H., Yuan, J., Cao, D. and Liu, P. L.-F. (2021) Wave overtopping flow striking a human body on the crest of an impermeable sloped seawall. Part II: numerical modelling. Coastal Engineering, 168, 103892.

There may be differences between this version and the published version. You are advised to consult the publisher's version if you wish to cite from it.

http://eprints.gla.ac.uk/249159/

Deposited on: 10 August 2021

Enlighten – Research publications by members of the University of Glasgow
http://eprints.gla.ac.uk

Wave overtopping flow striking a human body on the crest of a sloped seawall. Part II: Numerical modelling

Hao Chen[a,b], Jing Yuan[a,*], Deping Cao[a], Philip Liu[a]

[a] *Department of Civil and Environmental Engineering, National University of Singapore, 1 Engineering Dr. 2, Block E1A 07-03, 117576, Singapore*
[b] *School of Engineering, University of Glasgow, Glasgow, UK*

Abstract

The present paper is the second of two companion papers on the investigations of wave overtopping flow striking a cylinder on the crest of a sloped seawall, which is the surrogate of a human body. This paper numerically examines the detailed characteristics of the inline force acting on the cylinder by using a volume-of-fluid (VOF) based Reynolds-Averaged Navier-Stokes (RANS) model. The model simulates wave propagation, breaking on the seawall, overtopping and 3-dimensional interactions between the overtopping flow and the cylinder. The numerical model is carefully validated against the experimental data. Results show that the inline force generated by a plunging-breaker induced overtopping flows usually comprises a cycle of a first impact peak, a main peak and a secondary peak. However, for the inline force under surging-breaker induced overtopping flows, it is largely dominated by the main peak. The first impact peak is due to the impact of the tip of the overtopping flow on the cylinder, which usually has a higher flow velocity than the main stream. The main peak is generated by the asymmetric pressure distribution around the cylinder, which occurs when the main stream of overtopping flow passes the cylinder. As the inline force decreases after the main peak, there sometimes exists a secondary peak, which is formed by the complex free surface motion locally behind the cylinder. Additional numerical experiment is presented to demonstrate the applicability of a simple maximum inline force predictor developed in Part I. A prototype-scale simulation of irregular waves overtopping a sloped seawall is conducted to obtain the maximum inline force. The predictor also gives the maximum inline force in a wave-by-wave manner using the incident wave condition. These two approaches produce very similar estimates of maximum inline force, suggesting that the predictor can be used for engineering applications.

Keywords: Wave overtopping; Fluid-structure interaction; Impact force; Wave breaking.

*Corresponding author, e-mail address: nusyuan@gmail.com

November 18, 2020

1. Introduction

Wave overtopping is one of the major concerns in determining the effectiveness of coastal seawalls against flooding. Overtopping occurs when waves break and run up on the seaward slope of the seawall, reach the crest and pass over it. In designing a seawall, the key quantities describing wave overtopping are the mean overtopping discharge rate and the maximum overtopping volume, which must be limited below certain thresholds. These quantities can be obtained by either existing empirical formulas (EurOtop, 2018; Altomare et al., 2016; Van der Meer et al., 2009; Molines et al., 2019; Van der Meer and Bruce, 2013), or physical model tests (Pullen et al., 2009; Romano et al., 2015).

In many regions, the crest areas of seawalls are nice attractions for visitors, and public access to the seawall crest is often allowed. Unfortunately, in recent years, it has been reported in a number of publications that severe wave overtoppings have resulted in injuries or deaths of pedestrians on seawall crest. Allsop et al. (2003) stated that between 1999 - 2002, at least 12 people were dead in UK as being swept by wave overtopping. To gain insights of these tragedies, it is necessary to have a good understanding and modelling capability on how overtopping flows mobilize a pedestrian. Strictly speaking, neither the overtopping discharge rate nor the overtopping volume can directly explain how the overtopping flow endangers a pedestrian, though they have been used in some risk management guidelines for simplicity. Based on a variety of human stability experiments conducted in channel flume (Martínez-Gomariz et al., 2016; Russo et al., 2013; Jonkman and Penning-Rowsell, 2008), it is suggested that the hydraulic variables that define the flooding hazard posed to humans are the flow depth and velocity, which essentially determine the inline force on the human body. Therefore, these physical quantities are of particular interests in this paper, and they are the focus of the literature review below.

There are a number of publications discussing the overtopping flow depth and velocity by employing empirical formulas (Schüttrumpf and Oumeraci, 2005; Mares-Nasarre et al., 2019; Bosman et al., 2009; Van Bergeijk et al., 2019). These formulas are easy to use, and the empirical parameters in the formulas are calibrated based on the model-scale experimental data. However, each of these formulas has a clear range of applicability in terms of wave conditions, foreshore and slope angle of seawall. It is not always certain if these formulas are applicable for the conditions outside of their range of applicability. On the other hand, the experimental data on the velocity of overtopping flow is very limited. The main reason is the difficulty of obtaining reliable measurements, as the overtopping flow is generally very shallow, highly transient, and can be very aerated. Two companion papers (Ryu et al., 2007; Ryu and Chang, 2008) reported the laboratory measurements on wave overtopping on a rectangular structure. The particle image velocimetry (PIV) and bubble image velocimetry (BIV) were employed to measure the velocity, and the fiber optic reflectometer (FOR) was employed to measure the void fraction. In addition, dimensional analysis was performed and a formula was derived and calibrated for horizontal velocity along the deck. Similarly, in Chuang et al.

(2015, 2018), the highly aerated overtopping flow on a box-shaped structure was measured by the BIV. The overtopping flows were created by focused wave groups impinging on the front wall or directly on the deck. The velocities of the overtopping flow were successfully extracted and their relation to the impingement point was analysed.

In recent years, there have been a few publications on the investigations of overtopping flow striking onto structures near the coastal lines. Chen et al. (2015) developed an empirical formula for the overtopping loads on a vertical wall as a function of incoming wave conditions and seawall geometry. The formula was based on the concept of momentum flux, and several coefficients were introduced and calibrated based on scaled wave-flume experiments with a sloped (1:3 and 1:6) seawall. Further investigations were performed in Chen et al. (2016) for the maximum impact force on a wall induced by irregular-wave overtopping over a sloped seawall with a shallow foreshore. Van Doorslaer et al. (2017) developed design formulas for non-breaking wave overtopping and impacts on a storm wall. Three different approaches were suggested to calculate the impact forces on the wall, and their advantages and disadvantages were discussed. Large-scale laboratory tests have been performed by De Rouck et al. (2012) for breaking wave overtopping and impact on a storm wall. A so-called church-roof profile was reported for the recorded pressure and force on the wall, which shows a double-peaked shape for one impact event. Besides wind-generated waves, the impact force due to tsunami bore was also investigated in several research publications (Shafiei et al., 2016; Kihara et al., 2015). The bore was mostly generated by dam break wave in these laboratory tests, and several phases during the impact process were identified and their characteristics were analysed. Yeh (2006) computed the drag force on a cylinder in the tsunami runup zone, where the flow velocity was extracted based on the solution of shallow water equation, and a drag coefficient was needed for computation of the drag force.

Numerical methods have been under fast development in the past decades and a variety of numerical models have been proposed to model wave overtopping process. The model performance depends on the solved equations and solving technique, and relies heavily on a thorough verification and validation process (Losada et al., 2008). Nonlinear shallow water equation (NSWE) has been widely used to predict wave overtopping in e.g., Hu et al. (2000); Stansby and Feng (2004). The computational cost for such models is rather low, which makes them suitable for long-term modelling and statistical analysis. However, NSWE is derived based on the assumption of hydrostatic pressure distribution. Therefore, it has restrictions on modelling of wave breaking process, and the offshore boundary condition has to be located close to the seawall in order to satisfy the shallow water limit.

Alternatively, the Navier-Stokes solvers are becoming popular within the coastal engineering community due to the rapid growth of computational resources. This kind of solvers can directly simulate breaking waves and the complex interaction process between overtopping flows and structures without substantial approximations. They are more expensive with regard to the computational time, but still affordable with the aid of supercomputing facilities. They have been widely adopted to simulate wave breaking and wave-

structure interaction process with varying success (Lin and Liu, 1998; Xie, 2013; Bradford, 2000; Bakhtyar et al., 2009; Wang et al., 2009; Chella et al., 2016; Ghadirian and Bredmose, 2020; Paulsen et al., 2014). Limited works have also been published on the modelling of wave overtopping flow using this solver, most of which are 2-dimensional cases (Losada et al., 2008; Hsiao and Lin, 2010; De Finis et al., 2020). There still lack benchmark cases on 3-dimensional overtopping flow interacting with structures. Actually, this is more complex than the simulations of pure wave breaking or wave-structure interaction problems, because overtopping flow is a post-breaking flow with small thickness and fast speed. Adequate resolution of the impingement of such flow onto the structures requires the solver to be sufficiently accurate and robust.

This paper is the second of two companion papers. In the first paper Cao et al. (2020) (hereafter referred to as Part I), we described the results from an experimental study, and derived an empirical predictor for quick estimation of the inline force due to overtopping flow. In the present paper, we shall numerically model the breaking wave induced overtopping flow interacting with a cylinder at the edge of the seawall, which is the surrogate of a human body standing on the seawall crest. A volume of fluid (VOF) based Reynolds Averaged Navier-Stokes (RANS) solver is chosen in the present work. The primary goals of the paper are: (1) Thorough examination of the numerical model performance on dealing with such type of flow; (2) Detailed investigation of the physical process of the inline force on the cylinder; (3) Enlargement of the dataset for calibrating the empirical predictor proposed in part I; (4) Confirming the applicability of the empirical predictor for field conditions.

The remainder of the paper is organised as follows. In Section 2, the governing equations of the numerical model are described. Then in Section 3, the model results are validated against the experimental data with regard to the wave breaking on seawall slope, the overtopping flow and the inline force on the cylinder. In Section 4, detailed investigations of the inline force are provided. The temporal variations of the inline force are analysed and the underlying physics are investigated. A case study at a prototype scale is presented in Section 5, which involves irregular incident waves. Finally, conclusions of this paper are given in Section 6.

2. Governing equations

A two-phase flow solver in the open source toolbox OpenFOAM is utilised as the numerical model, which models both the air and water phases. The governing equations for the solver are the continuity equation and the Reynolds Averaged Navier-Stokes (RANS) equations

$$\frac{\partial u_i}{\partial x_i} = 0, \tag{1}$$

$$\frac{\partial \rho u_i}{\partial t} + \frac{\partial \rho u_i u_j}{\partial x_j} = -\frac{\partial p}{\partial x_i} - g_j x_j \frac{\partial \rho}{\partial x_i} - \frac{\partial}{\partial x_j}\left(2\mu S_{ji} + \tau_{ji}\right), \tag{2}$$

where x_i is the Cartesian coordinate system where $i = (1, 2, 3)$, u_i is the Reynolds averaged velocity, g_i is the gravitation vector, ρ is the density, p is the pressure in excess and μ is the dynamic viscosity. α is the water volume fraction and $\alpha \in [0, 1]$. Thus, the volume fraction of air is given by the complementary fraction $1 - \alpha$. The shear strain rate S_{ij} is defined as

$$S_{ij} = \frac{1}{2}\left(\frac{\partial u_i}{\partial x_j} + \frac{\partial u_j}{\partial x_i}\right), \tag{3}$$

and the Reynolds stress τ_{ij} is calculated according to the Boussinesq approximation

$$\tau_{ij} = -\rho\overline{u_i' u_j'} = 2\mu_T S_{ij} - \frac{2}{3}\rho k \delta_{ij}, \tag{4}$$

where the prime superscript denotes the turbulence fluctuations and the overbar signifies Reynolds-averaging process. k is the turbulent kinetic energy, δ_{ij} is the Kronecker delta, and μ_T is the eddy viscosity. A standard $k - \omega$ SST turbulence model is employed in the numerical model, which essentially models the turbulent kinetic energy k and the specific dissipation rate ω.

The free surface waves are generated by the waves2Foam toolbox developed by Jacobsen et al. (2012), which uses relaxation zones to induce incident gravity waves. The free surface is captured by using the concept of volume of fluid (Hirt and Nichols, 1981), where the water volume fraction field α is used to implicitly indicate the free surface position. The instantaneous local density and dynamic viscosity are specified in terms of the water volume fraction by the following constitutive equations

$$\begin{aligned} \rho &= \alpha\rho_w + \rho_a(1 - \alpha), \\ \mu &= \alpha\mu_w + \mu_a(1 - \alpha), \end{aligned} \tag{5}$$

where the subscript w and a refer to water and air, respectively. The isoAdvector approach proposed in Roenby et al. (2016) was adopted to advect the free surface, which is essentially an efficient two-step geometric VOF solver. In the first step, the free surface is explicitly reconstructed within each cell by applying the concept of isosurface. Secondly, from the reconstructed surface, the motion of the intersection lines between the cell face and the free surface is modelled to obtain their time evolution within a time step of the submerged face area. Readers are referred to Roenby et al. (2016) for details of the algorithm.

The numerical solution from RANS model provides field quantities e.g., the water volume fraction, pressure and velocity distribution over the domain. Since the inline force on the cylinder is resulted from both the pressure and the surface shear stress in the present model, it is obtained by directly integrating the pressure and the surface shear stress over the instantaneous wet surface S_b as

$$F_i = \iint_{S_b} p \, \mathrm{d}S_i + \iint_{S_b} (2\mu S_{ji} + \tau_{ji}) \cdot \, \mathrm{d}S_j. \tag{6}$$

It should be mentioned that although the isoAdvector method used in the numerical model is a geometric VOF method, it only reconstructs a temporary free surface within each time step. This free surface is not

Table 1: Test conditions in the experiments in Part I. h is the still water depth, R_c is the freeboard, H is incident wave height, T is the wave period and I_b is the Iribarren number.

h [m]	R_c [m]	H [m]	T [s]	I_b [-]
$0.65 \sim 0.95$	$0.05 \sim 0.35$	$0.069 \sim 0.209$	$1.2 \sim 3$	$1.33 \sim 4.04$

continuous and it is solely used for advecting free surface in the intermediate steps of the algorithm. It is not stored in the final solution, and the interface is finally represented implicitly by α. A native utility included in waves2Foam was used to extract the surface elevation η

$$\eta = \int_{z_{\alpha=1}}^{z_{\alpha=0}} \alpha \, \mathrm{d}z + z_{\alpha=1}, \tag{7}$$

where the integration of volume fraction was performed in a vertical line, and the free surface was located in-between the integration limits, i.e., $z_{\alpha=0}$ and $z_{\alpha=1}$. Actually, in Eq. (7), the position of free surface is averaged as the height of the water column above the level $z_{\alpha=1}$.

3. Model setup and validations

3.1. Brief review of the laboratory experiments in Part I

In this section, we briefly review the setup of the experiments and some of the important experimental observations reported in Part I. A set of experiments were conducted in a wave flume in the Hydraulic Laboratory at National University of Singapore. This wave flume is 36 m long, 1.3 m deep and 2 m wide. A piston-type wavemaker (HR Wallingford) was located at one end of the flume, and the seawall model with a 1:3 slope was constructed at the other end of the flume. The incident wave conditions used in the experiments are presented in Table 1. Four capacitance type wave gauges CG1 - CG4 were installed to measure the surface elevations at a few selected locations in front of the seawall, and four ultrasonic probes US1 to US4 were used to measure the depth of the overtopping flow on the seawall crest. A cylinder, as a surrogate of human body, was placed on the seawall crest. The cylinder was made of plastic pipe with an outer diameter of 6 cm, which gives a geometric scale of approximately 1:5. The upper end of the cylinder was mounted to a three-axis force sensor, which was bolted onto a rigid bar sitting on top of the flume. There was a tiny gap between the bottom of the cylinder and the seawall surface so that the cylinder did not touch the seawall surface during the experiment.

A definition sketch of the present problem is given in Fig. 1. The incident wave is characterised by the wave height H and wave period T. β is the slope angle of the seawall. The free board R_c is the difference between the seawall crest level and the still water level. d_{0m} is the maximum overtopping flow depth during one overtopping event. Based on a simple dimensional analysis, the governing parameters for the inline force on the cylinder are the relative freeboard R_c/H and the Iribarren number I_b, which is

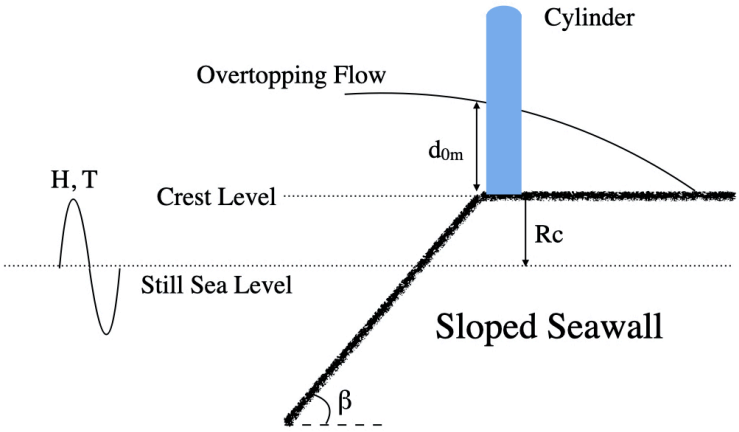

Figure 1: Definition sketch of overtopping flow interacting with a cylinder on the seawall crest.

defined as $I_b = \tan\beta/\sqrt{H/L_0}$ where L_0 is the deep water wave length. Given the incident wave conditions in Table 1, the main breaker type in the experiments is plunging breaker. However, for the cases with I_b close to or larger than 3.3, the wave tends to break with the features of surging breaker. Due to quite distinct behaviours of plunging and surging breakers, the resulted overtopping flows are rather different, which were clearly observed from the experiments. Therefore, in the analysis below in Section 3.3 and Section 3.4, the convergence and validation tests will be presented separately for both surging and plunging breakers. A representative case for surging breaker is chosen with $H = 0.20$ m, $R_c = 0.15$ m and $T = 3$ s. For the plunging breaker, the wave period of the representative case becomes 2 s and the other two parameters remain the same. The presentation of our numerical simulations will be largely based on these two representative cases.

3.2. Model setup

The numerical model was set up to reproduce the experiments in Part I. The domain has a length of 7.5 m from the left inlet boundary to the toe of the seawall. The width and height of the domain are 0.6 m and 1.3 m, respectively. The seawall was modelled as a smooth and impermeable slope with a height of 1 m and length of 3 m. A circular cylinder was located on the edge of the seawall, which is exactly the same as in the experiments. A relaxation zone was arranged in the left part of the numerical wave tank, starting from the inlet boundary and ends at 1.5 m to the toe of the slope. Within this relaxation zone, the waves were driven according to the stream function wave theory, and the velocity field u and the volume fraction field α were updated at each time step according to the relaxation function. At the right end of the numerical wave tank on the seawall crest, another short relaxation zone of 1 m was also applied to absorb the overtopping flow.

An example of the side view of the numerical wave tank is presented in Fig. 2 with zoom-in views of the mesh at some specific locations. A block-structured mesh with 18 blocks was generated using the

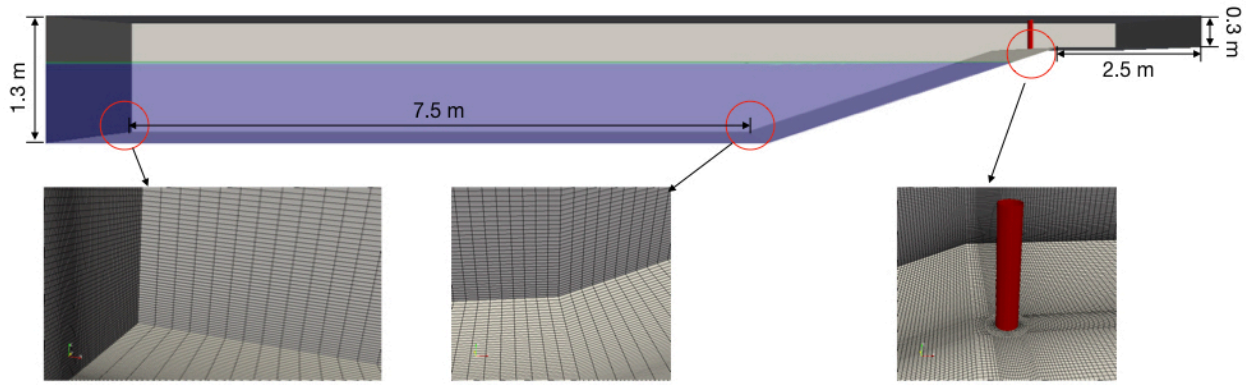

Figure 2: Overview of the numerical wave tank with zoom-in views of the block-structured mesh used in the numerical model. The purple area is the space initially occupied by the still water with a water depth of 0.85 m.

native blockMesh toolbox, which is distributed within the OpenFOAM toolbox. Before waves arrive at the toe of the slope, the grid only needs to resolve the large-scale wave propagation. Therefore, the grid in the wave-making zone is relatively coarse. On the slope, the waves start to shoal and eventually break, which produces the overtopping flow and further interacts with the cylinder. These hydrodynamic processes require a fine mesh to resolve. Hence, from the toe, the mesh is smoothly squeezed towards the cylinder. In the right relaxation zone, the grid is coarsened again as it is far away from the area that is of interest to us.

3.3. Mesh resolution and convergence

The total mesh number used in the present numerical model is 3.1 million. This mesh resolution can reasonably resolve the waves before wave breaking, since the horizontal resolution reaches around 130 cells per wave length and the vertical resolution reaches 12 cells per wave height. Near the cylinder, the grid resolution is further refined. The maximum overtopping flow depths for the two representative cases are about 0.05 m and 0.09 m, respectively. They are resolved by 22 cells and 40 cells vertically, so the main behaviour of the overtopping flow is expected to be correctly resolved.

Wave breaking on the seawall slope may lead to an aerated overtopping flow. Though our model utilises a two-phase flow solver, correct description of the evolution of these bubbles requires considerably finer mesh, and it is beyond the capability of the supercomputers to model such detailed flow in such a large scale. In this problem, the size of the entrained bubble is typically comparable to or even much smaller than the grid size. As will be shown in Section 3.4.1, the selected grid size still allows a good description of the big air cavity produced by a plunging wave breaker on the seawall slope (the scale of the cavity is $\mathcal{O}$(10 cm)). Regarding the boundary layer of the overtopping flow, its thickness can be roughly estimated by the flat plate theory. Consider the case with a plunging breaker, the characteristic velocity of the overtopping flow is about 2.0 m/s. This results in a boundary layer thickness of approximately 2 mm at 0.5 m away from the breaker location. The thickness of the boundary layer is very similar to the height of the first

Table 2: Mesh parameters for the convergence study. The cell size in the wave-making zone is the averaged size at the free surface area, as there is a smooth refinement from the far end near the wave-maker boundary to the area near the seawall. The cell size in the near-cylinder zone is the size of the first layer cell above the seawall's crest near the cylinder.

Grid NO.	Wave-Making Region		Near-Cylinder Region			Mesh NO. [million]
	Δx [mm]	Δz [mm]	Δx [mm]	Δy [mm]	Δz [mm]	
1	66	21	4.8	4.8	2.6	1.86
2	56	18	4.1	4.1	2.2	3.10
3	48	15	3.5	3.5	1.9	5.14

layer of the grids. Although a wall function was applied in the model to help describe the flow inside the boundary layer, it is not guaranteed that the boundary layer was adequately modelled. Nevertheless, the effect of boundary layer is generally negligible for our overtopping-flow-cylinder interaction, so it is not really necessary to refine mesh for the purpose of modelling boundary layers.

To demonstrate the adequacy of the computational mesh resolution, a convergence test was performed to verify the sensitivity of the overtopping flow depth and the inline force on the grid resolutions. The two representative cases introduced in Section 3.1 were simulated using three different resolutions, i.e., the current mesh resolution used in our simulations (Grid 2), a coarser mesh of 1.8 million cells (Grid 1) and a finer mesh of 5 million cells (Grid 3). The details on the size of these three grids are given in Table 2. These three different grids are geometrically similar between each other, and the results from the test are presented in Fig. 3. Regarding the overtopping flow depth shown in Fig. 3(a), the time series for the surging-breaker case are quite smooth, and they agree with each other very well. For the plunging-breaker case, there are considerable high-frequency fluctuations. Such fluctuations are due to the entrained air bubbles, since the overtopping flow is highly aerated in this case. As described in Section 2, the elevation of free surface is obtained using Eq. (7), which represents an average height of the free surface over the vertical water column. Therefore, whenever the entrained air bubbles pass through the location of observation, there can be a sudden drop for the surface elevation, as shown in e.g., $t = 7.2$ s for Grid 2. Due to the limited resolution, none of the grid resolutions can capture the bubbles adequately. Hence the finest mesh does not necessarily give the best representation of the free surface. Despite of the high-frequency fluctuations, the general shape and the peak of the flow depth are about the same among the three predictions. Thus, the numerical results are convergent in terms of the overtopping flow depth.

To facilitate the discussions on the convergence of the inline force, a few terms are defined first, which are used to describe the temporal variations of the inline force. Fig. 4 presents a typical time series of inline force on the cylinder of one overtopping event from the plunging-breaker case. There may exist multiple peaks within one cycle, but there are three peaks that we are most interested in, namely the first impact

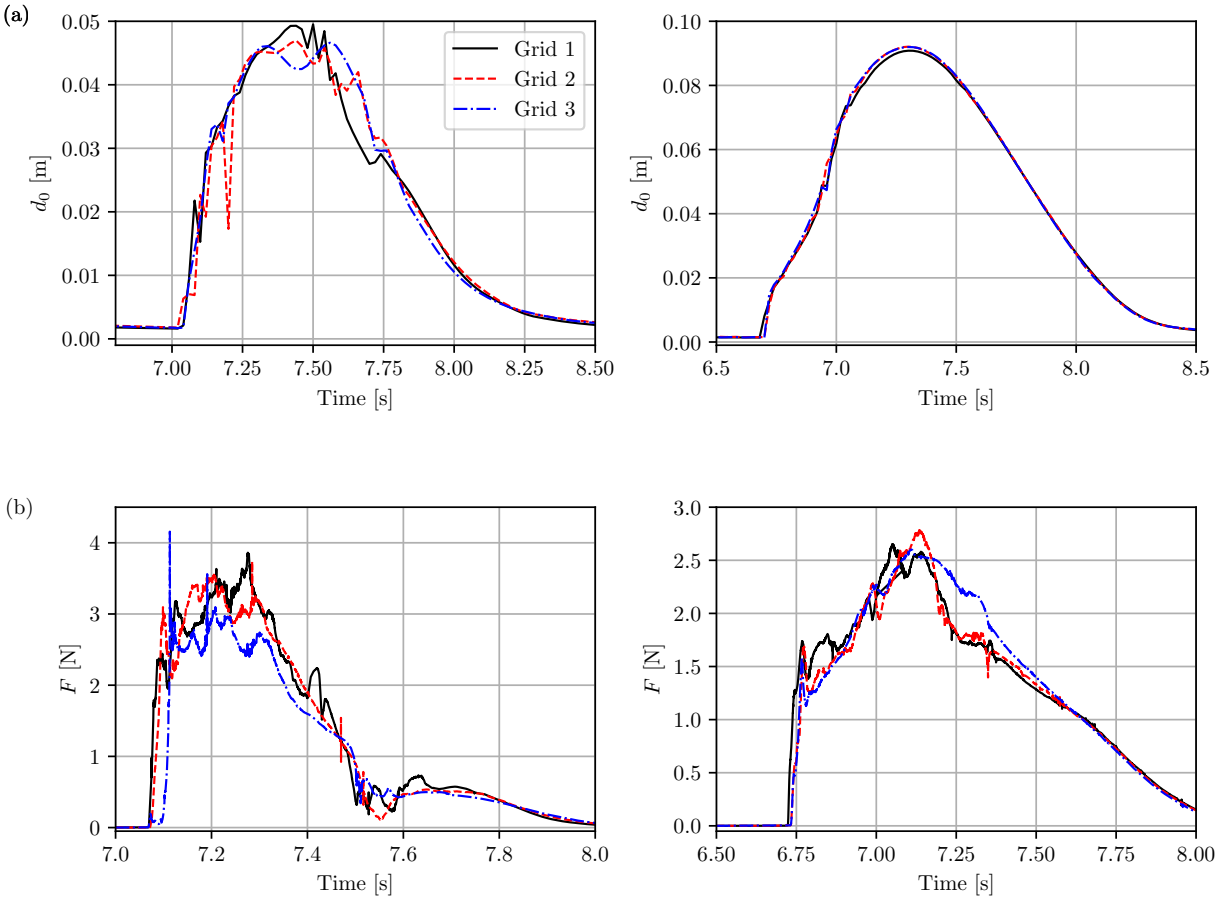

Figure 3: Results from the convergence test. (a) Computed depth of the overtopping flow at the leading edge of the seawall crest using different grid resolutions. (b) Computed inline force on the cylinder using different grid resolutions. The incident wave conditions are $H = 0.20$ m and $R_c = 0.15$ m. Left: plunging-breaker case ($T = 2$ s). Right: surging-breaker case ($T = 3$ s).

peak, the main peak and the secondary peak. Define the nondimensional time $t' = (t - t_0)/(R/U_m)$ where R is the radius of the cylinder, U_m is the maximum depth-averaged velocity of the overtopping flow during this overtopping event and t_0 is the starting time of the inline force due to overtopping flow. The first impact peak occurs when the tip of the overtopping flow touches the cylinder at $t' = 2.24$. The duration for this peak is extremely short and the force is rapidly reduced after this peak. The main peak occurs around $t' = 5.55$, and it is due to the interaction of the main stream of the overtopping flow with the cylinder. The duration of this peak is considerably longer than the first impact peak, and there can exist multiple local peaks around the main peak due to e.g., entrained air bubbles or surface ripples. During the decrease stage of the inline force, there exists a secondary load cycle, starting with the dip at $t' = 26.7$ and reaches its maximum around $t' = 30$. We refer this phenomenon as the secondary load cycle and its associated peak

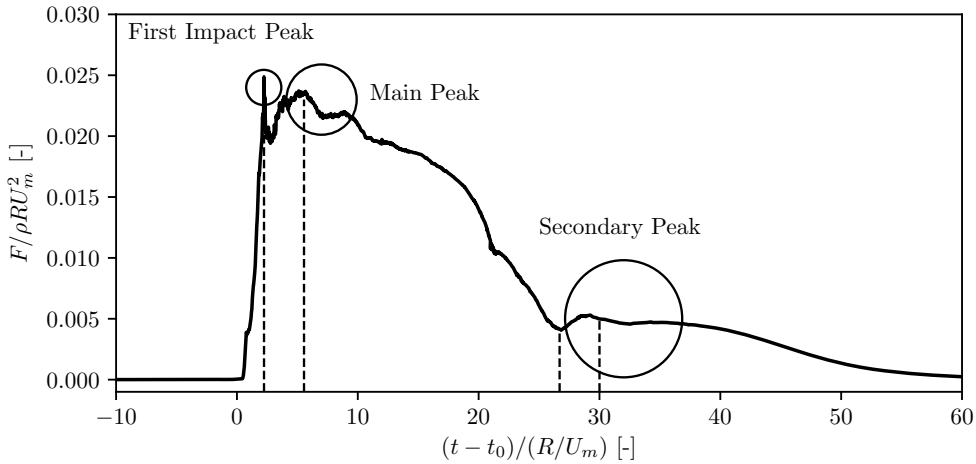

Figure 4: Illustration of the first impact peak, the main peak and the secondary peak within one overtopping event. The prediction is from the plunging-breaker case for one typical overtopping event. The four dashed vertical lines denote the time instants at $t' = 2.24$, $t' = 5.55$, $t' = 26.70$, $t' = 30.0$, respectively.

is called the secondary peak. Detailed investigations and discussions on these three peaks will be given in Section 4.

Fig. 3(b) compares the inline force under different grid resolutions. Comparing to the prediction of surface elevation in Fig. 3(a), the effect of mesh size on the inline force seems to be more pronounced. For the plunging-breaker case, the three grids give very different first impact peak, and the main peak's magnitudes also seem to reduce as the mesh being refined, i.e., the main peak drops from about 3.5 N for Grid 1 to 3.0 N for Grid 3. As mentioned above, the overtopping flow in this case is highly aerated. The flow's irregularity due to the entrained air phase produces significant fluctuations in the predicted inline force. This effect is most pronounced during the early stage of an overtopping event, since the front of the overtopping flow is more aerated than the tail. This explains the discrepancies in the predictions of first-impact peak and the main peak. The second load peak, on the contrary, varies little with the grid resolution, and this is largely because the local flow has become much 'greener' when the secondary peak occurs. For the surging-breaker case, the agreement among the three predictions seems to be much better than that for the plunging-breaker case. This is mainly because the overtopping flow of the surging breaker is much less aerated. Since the numerical model cannot loyally capture the evolution of entrained air, a finer resolution does not necessarily give better prediction of the entrained air phase.

Generally speaking, the three grid resolutions give very similar overall temporal variation of the inline force, and the discrepancy for the main peak (the target parameter of interest to us) is around 10%, which is small enough for our application. Thus, we consider that Grid 2 is fine enough to give a reasonable prediction of both overtopping flow and inline force.

3.4. Model validations

3.4.1. Wave breaking

In this section, we examine the model performance on the wave breaking process. The primary focus is on the plunging-breaker case, as it involves much more complex process than surging-breaker case, e.g., strong free surface deformation and impingement of plunging jet on the slope of the seawall. The snapshots of wave breaking process from the experiments in Part I and the numerical model are given in Fig. 5. In Fig. 5(a), the free surface starts to overturn and leads to the formation of a plugging jet, as shown in Fig. 5(b). At the beginning of the impingement, the tip of the plunging jet touches the seawall slope, and a big air pocket is trapped inside the flow (Fig. 5(c)). The impingement turns the plunging jet into a violent water splash, and the trapped air pocket collapses and evolves into a breaking roller (Fig. 5(d)). Subsequently in Fig. 5(e), the water splash is organized into a runup jet along the seawall surface, which is highly aerated and has a very high speed.

By comparing with the observations, it is seen that the numerical model is capable to describe the overall process of the plunging wave breaking, including the formation of the plunging jet flow, the impinging process and the subsequent roller. However, the highly aerated overtopping flow cannot be captured by the numerical model. In the experiments, air bubbles are distributed throughout the runup jet, so the flow appears 'white'. However, this is not fully reflected in the numerical results.

3.4.2. Overtopping flow

The overtopping flow depth and velocity are of interests in the present paper, as introduced in Section 1 that they are directly related to the inline force on the cylinder. They were sampled at the edge of the seawall at 0.1 m from the side wall, thus the disturbance of cylinder on the overtopping flow is negligible. Regarding the overtopping flow depth, the numerical results were obtained based on Eq. (7), and experimental results were measured using the ultrasonic probes. Direct comparison of the time series of the overtopping flow depth at the edge is presented in Fig. 6. The comparison shows a rather good agreement for the surging-breaker case. For the plunging-breaker overtopping, both results show oscillations due to the entrained air, which has been explained in Section 3.3. In general, the maximum overtopping flow depth is predicted well by the model.

In Fig. 7, a few vertical velocity profiles for the overtopping flow of the plunging-breaker case are presented at different time instants during one specific overtopping event. It should be mentioned that the numerical results are generally quite repeatable and cycle variation is not significant, so it is not necessary to cycle-average the results. The instantaneous velocity and flow depth is nondimensionalised by the maximum depth-averaged velocity and the maximum flow depth during this event. It is found that initially when the tip of the flow just arrives at the edge of the seawall, the flow is largely non-uniform across the depth. The top layer has a faster flow velocity than the bottom layer. The flow velocity near the bottom rapidly accelerates

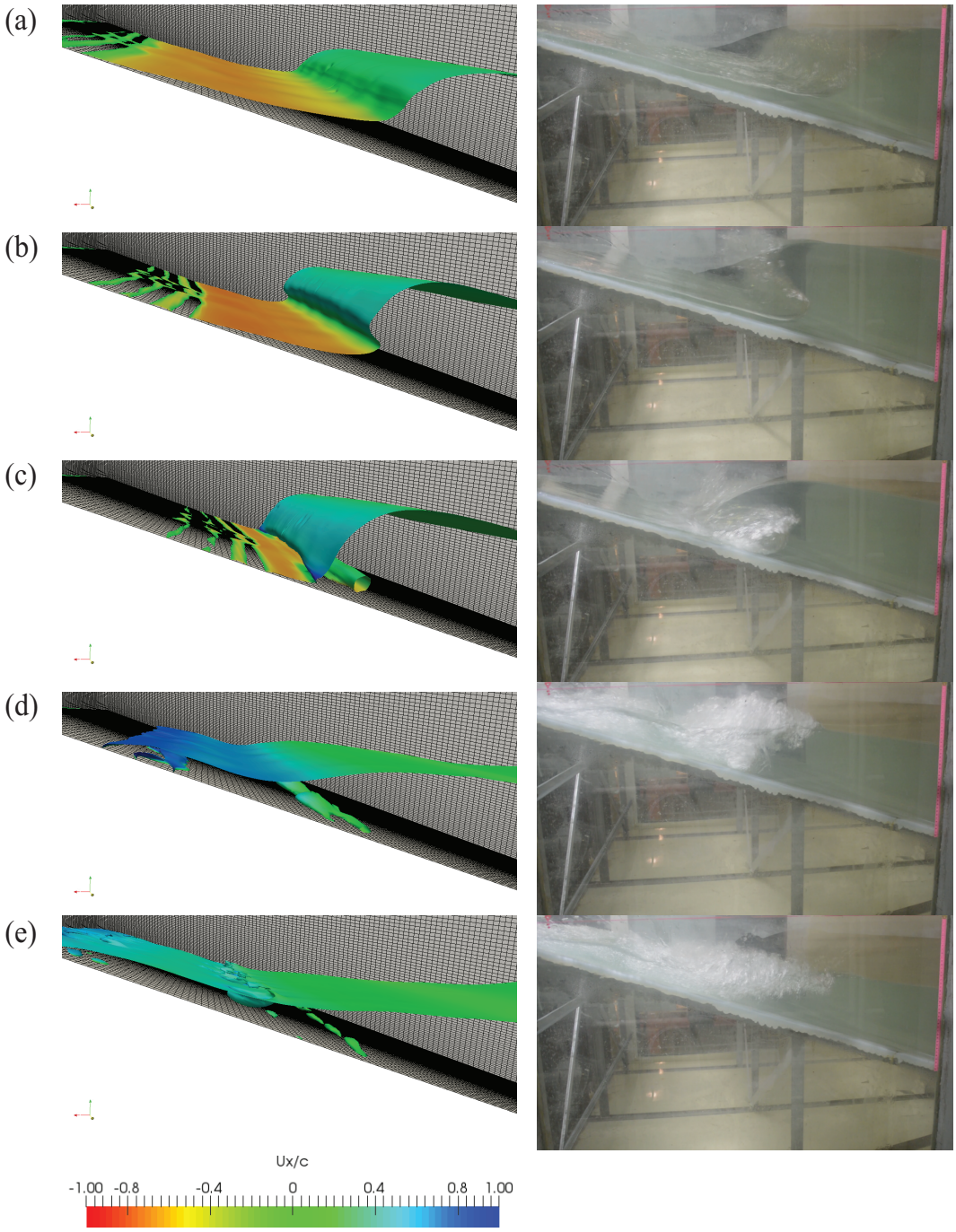

Figure 5: Snapshots of the plunging wave breaking process from the numerical simulations (left column) and the experiments (right column) at: (a) the time when the wave starts to overturn ($t_1 = 0$ s, $t_2 = 0$ s); (b) the time during the wave overturn ($t_1 = 0.14$ s, $t_2 = 0.18$ s); (c) the time when the overturned wave impinges the sloped seawall ($t_1 = 0.22$ s, $t_2 = 0.30$ s); (d) the time when the flow is strongly areated just after the impinge ($t_1 = 0.36$ s, $t_2 = 0.46$ s); (e) the time when the areated flow is further advected towards the seawall's crest ($t_1 = 0.46$ s, $t_2 = 0.64$ s). Here t_1 and t_2 are the time extracted from the simulations and the experiments, respectively. The free surface of numerical simulations is coloured with the horizontal velocity scaled by the wave celerity c.

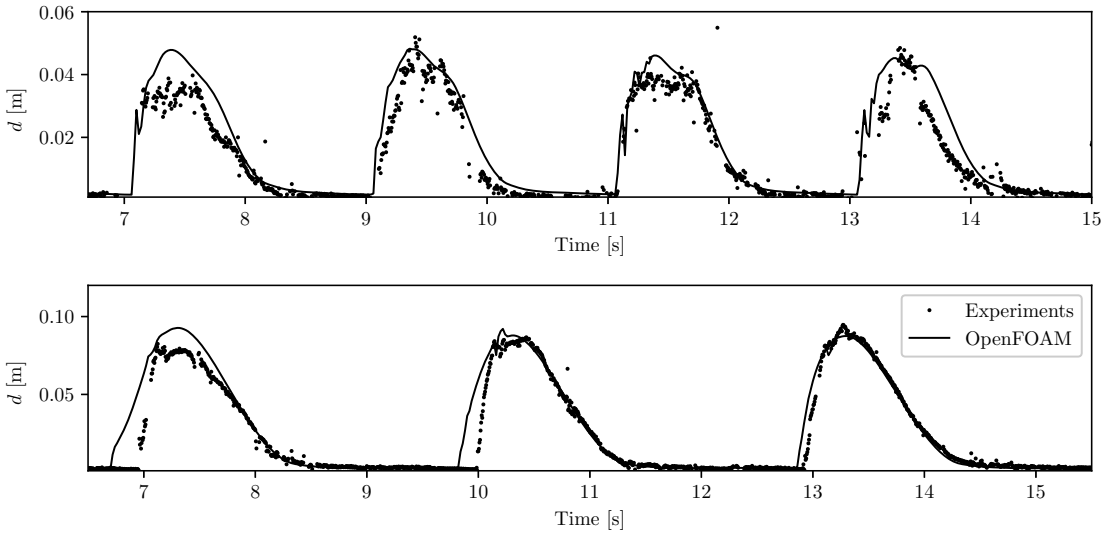

Figure 6: Comparison of the overtopping flow depth at the edge of the seawall for the cases with a plunging breaker (upper) and surging breaker (lower). The incident wave conditions are $H = 0.20$ m and $R_c = 0.15$ m. Upper: $T = 2$ s. Lower: $T = 3$ s.

and eventually the overtopping flow at the seawall's leading edge becomes almost uniform vertically before the depth reaches the maximum.

There is a difference between the occurrence time for the maximum depth-averaged flow velocity and the maximum flow depth. This is demonstrated in Fig. 8, which presents the time series of the overtopping flow depth d and the depth-averaged velocity U at the edge of the seawall for both the plunging and surging breakers. It is observed that there is a clear shift between the peak of the velocity and the peak of the flow depth. For both cases, the flow velocity rapidly reaches its maximum when the flow just arrives at the edge. With further development of the flow, its depth continues to grow until the maximum, while the flow velocity decreases continuously. Moreover, the shift for the plunging wave overtopping flow is more obvious than the surging wave overtopping. This is due to the different characteristics of the overtopping flow, which can be represented by the local Froude number defined as

$$F_r = \frac{U_m}{\sqrt{g d_m}} \tag{8}$$

The plunging breaker produces a supercritical flow with fast speed and very thin layer, while the surging breaker creates an overtopping flow with relatively slow speed and thick layer. This can be demonstrated by Fig. 9, which depicts the variation of Froude number against I_b under the same relative free board R_c/H. It is clearly seen that with the increase of I_b, the Froude number drops from very supercritical flow ($F_r = 2.75$) to nearly critical flow ($F_r = 1.25$).

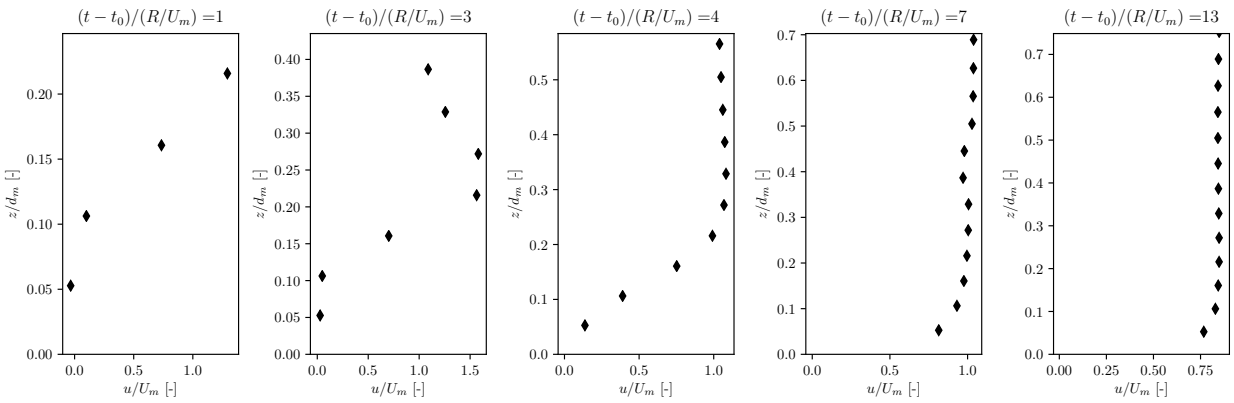

Figure 7: Evolution of the inline velocity profile for the overtopping flow of the plunging-breaker case at the edge of the seawall at 0.1 m from the side wall. d_m and U_m are the maximum flow depth and depth-averaged overtopping flow velocity within this specific overtopping event, respectively. t_0 is the time when the overtopping flow arrives the edge of the seawall. R is the cylinder radius. The wave condition for this case is $H = 0.2$ m, $T = 2$ s and $R_c = 0.15$ m and the selected wave cycle corresponds to the third wave cycle as shown in the upper subfigure in Fig. 6.

3.4.3. Inline force on the cylinder

Comparison between the predicted and measured inline forces on the cylinder is presented in Fig. 10. For the surging-breaker case, a small first impact peak is observed from the numerical results. However, it is mostly absent from the experiments. Instead, a single-peak time variation with moderate cycle-to-cycle difference is seen from the experimental results. Furthermore, there is an underestimation of the main peak of the force, which is about 15% $\sim$ 20%. On the other side, regarding the validation of inline force on the plunging-breaker case, we have several comments: (1) The first impact peak is more obvious in the numerical model, the magnitude of which seems to vary significantly among different wave cycles; (2) Underestimation of the main peak still exists, but is less significant than that for a surging breaker; (3) The secondary peak exists for both experimental and numerical results, but the experiment gives a larger value for the secondary peak.

4. Detailed investigations on the inline force

4.1. First impact peak

To illustrate the first impact peak, we extract a snapshot of the plunging-breaker case when the first impact peak occurs, and show them together with the time series of the inline force on the cylinder in Fig. 11. It is seen that the first impact peak is induced when the tip of the overtopping flow just slams onto the cylinder. On the cylinder's surface, a small area with a high effective pressure (over 2000 Pa) is created around the point of impact. The duration of the impact is extremely short, which is about $0.5(R/U_m)$, in the order of 0.001 s to 0.01 s.

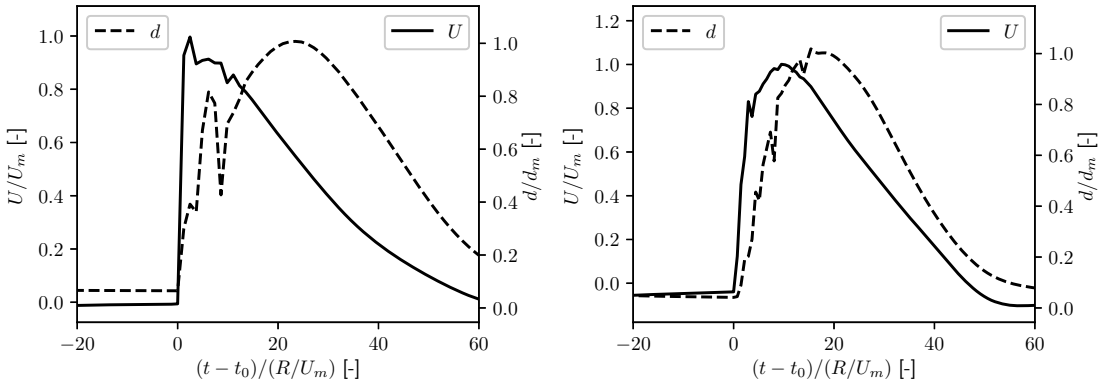

Figure 8: Time series of the overtopping flow depth and depth-averaged velocity profile at the leading edge of the seawall for one particular overtopping event. U is the depth-averaged velocity and the subscript m indicates the maximum value within this overtopping event. t_0 is when the overtopping flow arrives the edge of the seawall. Left: The plunging-breaker case ($T = 2$ s). The selected wave cycle corresponds to the third wave cycle in the upper subfigure in Fig. 6. Right: The surging-breaker case ($T = 3$ s). The selected wave cycle corresponds to the third wave cycle in the lower subfigure in Fig. 6.

The first impact peak is more obvious for the cases with plunging breakers, and it even may not occur for some surging-breaker cases. As introduced above, the plunging wave breaker produces a thin layer of flow with very fast speed. For example, the flow velocity in Fig. 11 is up to $2 \sim 3$ m/s, while the thickness of the flow is only a few millimetres at the tip. This naturally creates a condition for the first impact peak to occur. Furthermore, for the same case, the numerical model tends to predict a more obvious first impact peak than the laboratory tests, as shown in Section 3.4. One possibility is that in the experiments there was a tiny gap between the cylinder's bottom and the seawall crest's surface (a necessary configuration for measuring the in-line force). Therefore, the tip of the overtopping flow may partially pass beneath the cylinder in the experiments, which leads to a reduced first impact peak. Furthermore, deformation and vibration of the cylinder may also reduce the first impact peak. We also find a strong cycle-to-cycle variation for the first impact peak. This is not surprising, as we have argued that the first impact peak is associated with the local behaviour of the overtopping flow in the tip. In each overtopping cycle, the local shape and curvature of the tip can be different, leading to different magnitudes of the first impact peak.

We shall emphasise that in the context of overtopping flow-human interaction, a correct estimate of the first impact peak on the circular cylinder is secondary, since it is strongly related to the local curvature of the body, which can not be well represented by a simple cylinder. Furthermore, human body is not completely rigid, i.e., the muscle and skin are considerable flexible. Essentially, the finite stiffness of human body makes the problem associate with hydroelasticity. This is out of the scope of the present paper and further investigations are needed.

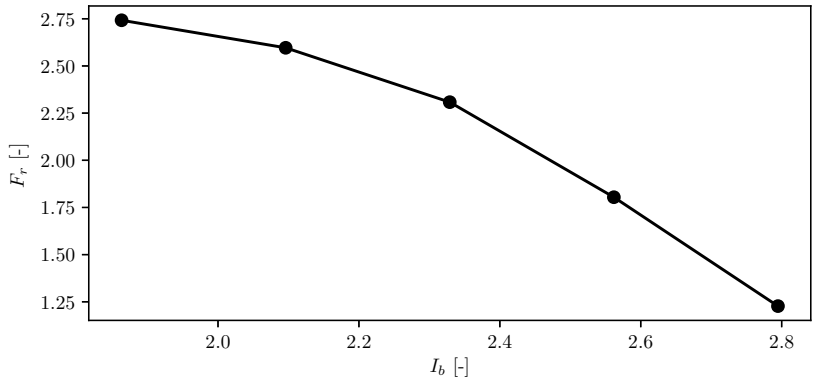

Figure 9: The local Froude number of the overtopping flow, defined by Eq. (8), versus the Iribarren number I_b. For all the data, $R_c/H = 0.75$.

4.2. Main Peak

The main peak is the consequence of the interaction between the cylinder and the main stream of the overtopping flow. By extracting the friction drag (integral of surface shear stress) and the form drag (integral of surface pressure) on the cylinder as shown in Fig. 12, it is concluded that for both the plunging-breaker and the surging-breaker cases, form drag is the main contributor to the total inline force on the cylinder. In other words, it is the difference between the pressure acting on the front and back sides of the cylinder that results in the inline force.

Fig. 13 presents the snapshots of the simulation for the surging-breaker case around the time when the main peak occurs. When the main body of overtopping flow hits the cylinder, water is piled up in front of the cylinder due to its blockage. Furthermore, there is a tiny runup jet flow climbing upwards along the cylinder. As the flow wraps around the cylinder, the free surface level drops continuously, so there is much less water in the wake region. As can be expected, the asymmetry distribution of immerse area around the cylinder leads to an asymmetry distribution of pressure acting on the cylinder's surface, as shown in the lower row in Fig. 13. The main peak occurs when this asymmetry is maximized.

To further demonstrate this, we perform vertical line integration of the total pressure on the cylinder's surface (from bottom to free surface), and present the distribution of this integrated pressure along the perimeter of the cylinder in Fig. 14. The integrated pressure on the front, i.e., $-45° < \phi < 45°$ is considerably larger than that on the back side at the moment of main peak ($t = 13.14$ s). With further development of flow, the integrated pressure on the front side decreases, while on the back side it increases. Therefore, the net inline force reduces after the main peak.

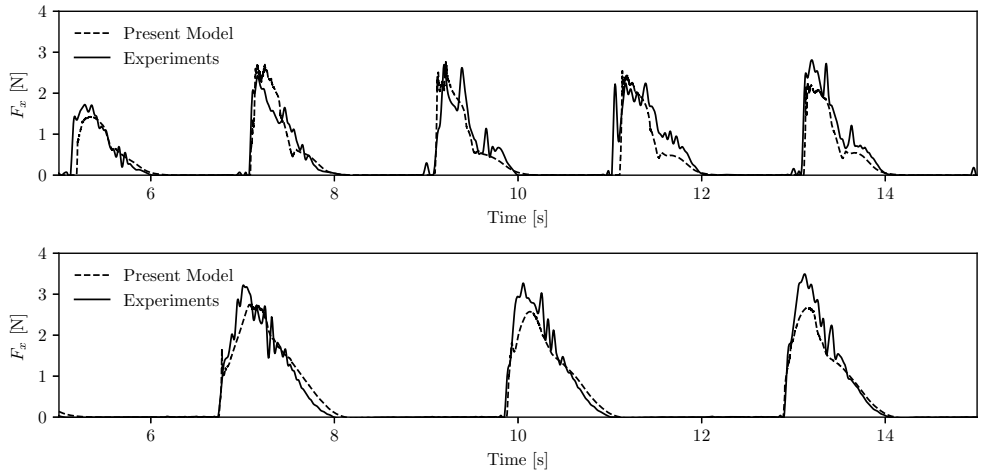

Figure 10: Comparison of the time series of the inline force on the cylinder due to plunging wave overtopping (upper) and surging wave overtopping (lower). The incident wave conditions are $H = 0.20$ m and $R_c = 0.15$ m. Upper: $T = 2$ s. Lower: $T = 3$ s.

4.3. Secondary load cycle

A secondary load cycle, which appears after the main peak (as illustrated in Fig. 4), is often observed for the cases with plunging breaker on the seawall slope. This feature of the inline force is strongly related to the local flow in the back side of the cylinder. Fig. 15 presents a few snapshots for the flow near the cylinder during the secondary load cycle for the plunging-breaker case. In Fig. 15(a) when the overtopping flow just passes the front side of the cylinder, the flow appears to be separated from the back of the cylinder, and a dry zone is formed behind the cylinder. Then the water quickly flows into the dry zone, and a small water column starts to build in the wake, as indicated by the circle in Fig. 15(b). The water column continues to grow in Fig. 15(c), which reaches its maximum in Fig. 15(d) and begins to fall down. Fig. 15(e) shows the collapsing of the water column, which lasts until the end of the second load cycle in Fig. 15(f).

As mentioned above, the water column is built due to the returned flow into the dry zone. This actually creates a positive pressure zone (pointing towards the cylinder) that partially counterbalances the inline force. This is confirmed in Fig. 16, which shows the distribution of the vertical pressure integral during the secondary load cycle. The secondary load cycle is found to be associated with the fall-down process of the water column in the back. The 'dip' of the inline force, which marks the beginning of the secondary load cycle, occurs at $t = 11.52$ s when the water column reaches its maximum. With the decreasing of the water column height, the pressure in the wake zone is further reduced, and this decay is faster than the decay of pressure force acting on the front side of the cylinder. This gives rise to an increased inline force, which appears to be a secondary cycle in the time series of the inline force.

Similar findings on the secondary load cycle have been documented in previous publications (Ghadirian

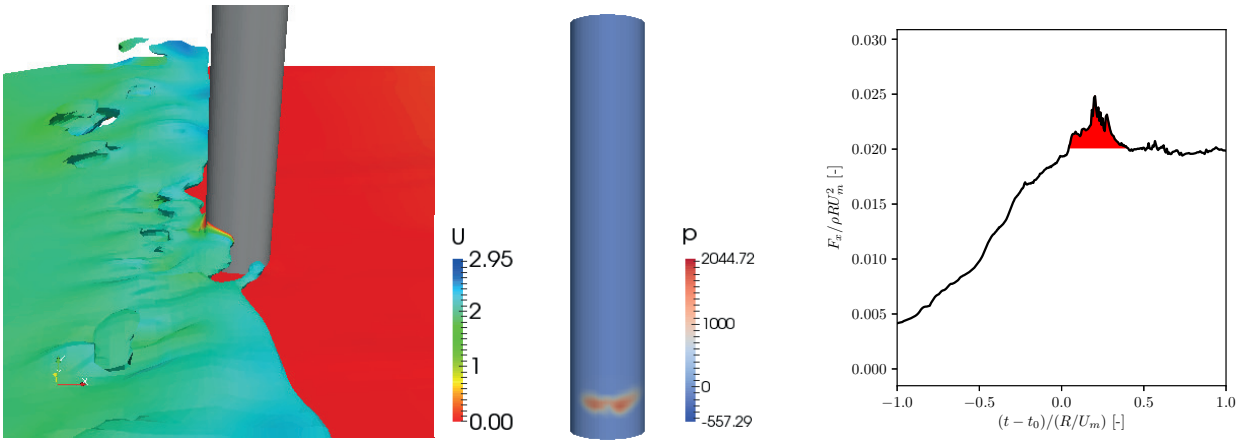

Figure 11: Illustration of the first impact peak. Left: A snapshot when the first impact peak occurs. Middle: Pressure field on the cylinder when the first impact peak occurs. Right: Inline force time series on the cylinder, where the effect of first impact peak is highlighted with red shaded area. t_0 is the time when impact occurs. ρ is water density.

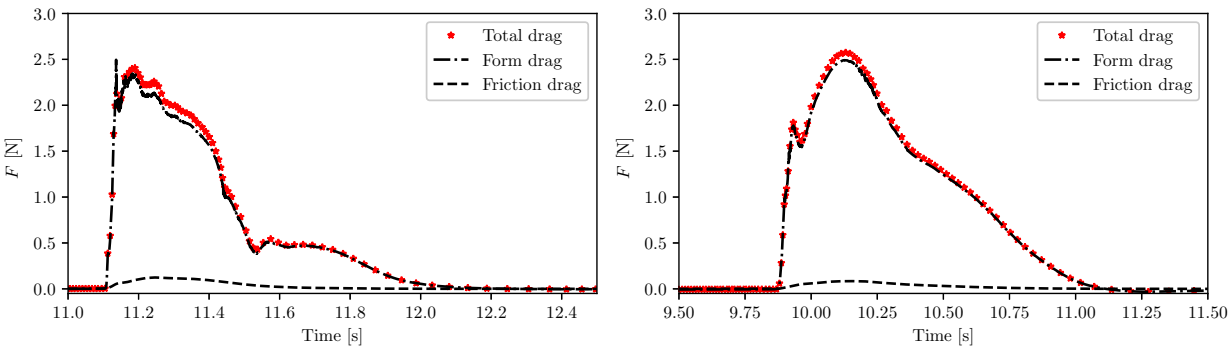

Figure 12: Comparison of the friction drag and form drag during one overtopping event. The incident wave conditions are $H = 0.20$ m and $R_c = 0.15$ m. Left: The plunging-breaker case ($T = 2$ s). Right: The surging-breaker case ($T = 3$ s).

and Bredmose, 2020; Paulsen et al., 2014; Riise et al., 2018) mainly in the context of wave-cylinder interaction. There is a strong analogy between these two contexts, as the secondary load cycle in both cases are related to the nonlinear free surface deformation behind the cylinder. In our case, there is a clear dry zone that is later on filled by the returned flow towards the front the cylinder. This explains why the secondary load cycle only occurs under steep plunging wave overtopping, as the local Froude number is high enough to provide a strong flow with high speed. This is the prerequisite for the flow separation and the dry zone to occur.

5. Predictor of maximum inline force

In Part I, a predictor has been developed for quick estimation of the maximum inline force F_{0m} acting on the human standing at the edge of the seawall crest. Here F_{0m} is scaled with the square of wave height.

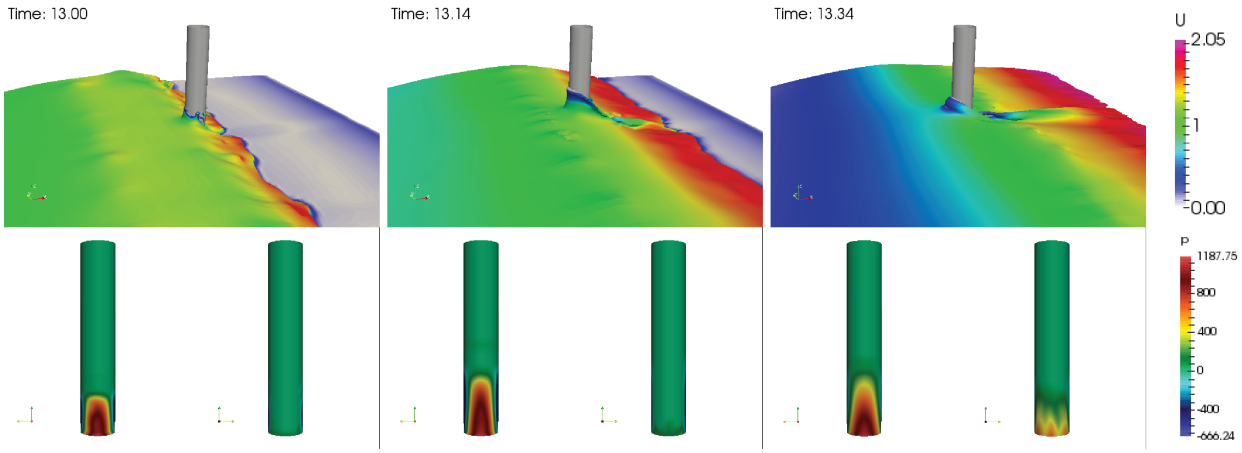

Figure 13: The snapshots of the flow (upper column) and the pressure distribution on the front and back side of the cylinder (lower column, left: front side, right: back side) before the main peak ($t = 13.00$ s), when the main peak occurs ($t = 13.14$ s), and after the main peak ($t = 13.34$ s). The results are from the surging-breaker case, and the incident wave condition is $H = 0.20$ m, $R_c = 0.15$ m and $T = 3$ s.

The scaling parameter C_H is determined by the relative freeboard R_c/H and I_b, and F_{0m} is calculated as

$$F_{0m} = C_H \left(I_b, \frac{R_c}{H} \right) \cot \beta \, \rho g H^2 D \tag{9}$$

where ρ, g are the density of water and gravitation, β is the slope of the seawall, D is the equivalent diameter, which is demonstrated to be about 70% of human waist width as shown in Part I.

The scaling parameter C_H was calibrated solely based on the model-scale experimental data in Part I under the slope of 1:3. Since in the present paper, the numerical model has been well validated, it is also applied to compute a vast amount of cases under the slope of 1:2, 1:3 and 1:4, in order to enlarge the dataset for calibration. The test conditions are summarised in Table 3. The model is applied in prototype scale by directly scaling up the mesh described in Section 3.2. It is expected that this resolution should be sufficient to capture the main peak, which is essentially dominated by inertia effects as shown in Section 4. Combining with the experiment dataset in Part I and the simulated data, the scaling parameter C_H is plotted as a function of R_c/H and I_b in Fig. 17. The data cloud in Fig. 17 is linearly interpolated onto a uniform R_c/H - I_b grid, covering R_c/H within $(0.5, 2)$ and I_b within $(1.1, 3.5)$. The interpolated $C_H = f(R_c/H, I_b)$ is provided in the supplementary materials of the present paper. We evaluate the accuracy of the interpolated C_H by applying it and the predictor to the cases in the calibration dataset. It is shown that 73% of the predicted F_{0m} have a discrepancy of less than $\pm 30\%$. Considering that the approximation of human body as an cylinder will inevitably introduce some uncertainties that is comparable to 30%, we consider this calibration of C_H and the predictor are accurate enough for our application.

In the following part of this section, we shall present a test of Eq. (9) against a numerical experiment at prototype scale. In the field, incoming waves are always irregular, and one way to deal with the irregularity is

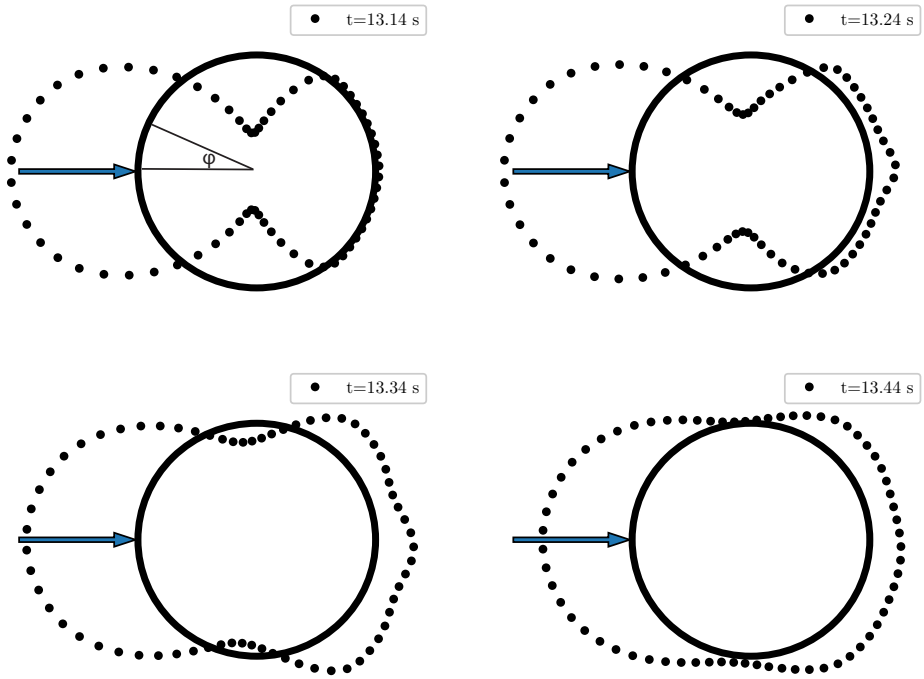

Figure 14: Distribution of the total pressure integration in the circumference direction from $\phi = 0°$ to $\phi = 360°$, where $\phi = 0°$ corresponds to the front stagnation of the cylinder. The pressure is integrated from the bottom to the instantaneous free surface. The dots outside the cylinder represent positive pressure integration i.e., acting into the cylinder, and vice versa. The results are from the surging-breaker case. The incident wave condition is $H = 0.20$ m, $R_c = 0.15$ m and $T = 3$ s.

Table 3: Test conditions in the numerical simulations at prototype scale.

h [m]	R_c [m]	H [m]	T [s]	I_b [-]
$2.5 \sim 3.5$	$0.5 \sim 1.5$	$0.4 \sim 1.6$	$3 \sim 6$	$1.1 \sim 3.5$

the so-called wave-by-wave approach. Namely, we treat a train of irregular waves as an ensemble of individual regular waves, so the force predictor can be applied wave-by-wave to quickly estimate the maximum inline force under each wave cycle. Coastal waves are often assumed to have a narrow spectrum, and the spreading of wave traveling direction is limited by wave refraction, so such a wave-by-wave approximation may work well. To test this idea, a numerical simulation is firstly conducted, in which irregular waves are normally incidented towards a sloped seawall. The mesh is the same as used in the calibration process, namely by scaling up the mesh in the model scale and the slope used here is 1:3. Using the high-fidelity numerical model, the inline force of a cylinder on the seawall's edge can be directly simulated, and the results are to be compared with those given by wave-by-wave applying the simple force predictor. The incident waves are divided into individual waves using zero-crossing method recorded at the offshore boundary. Therefore, for

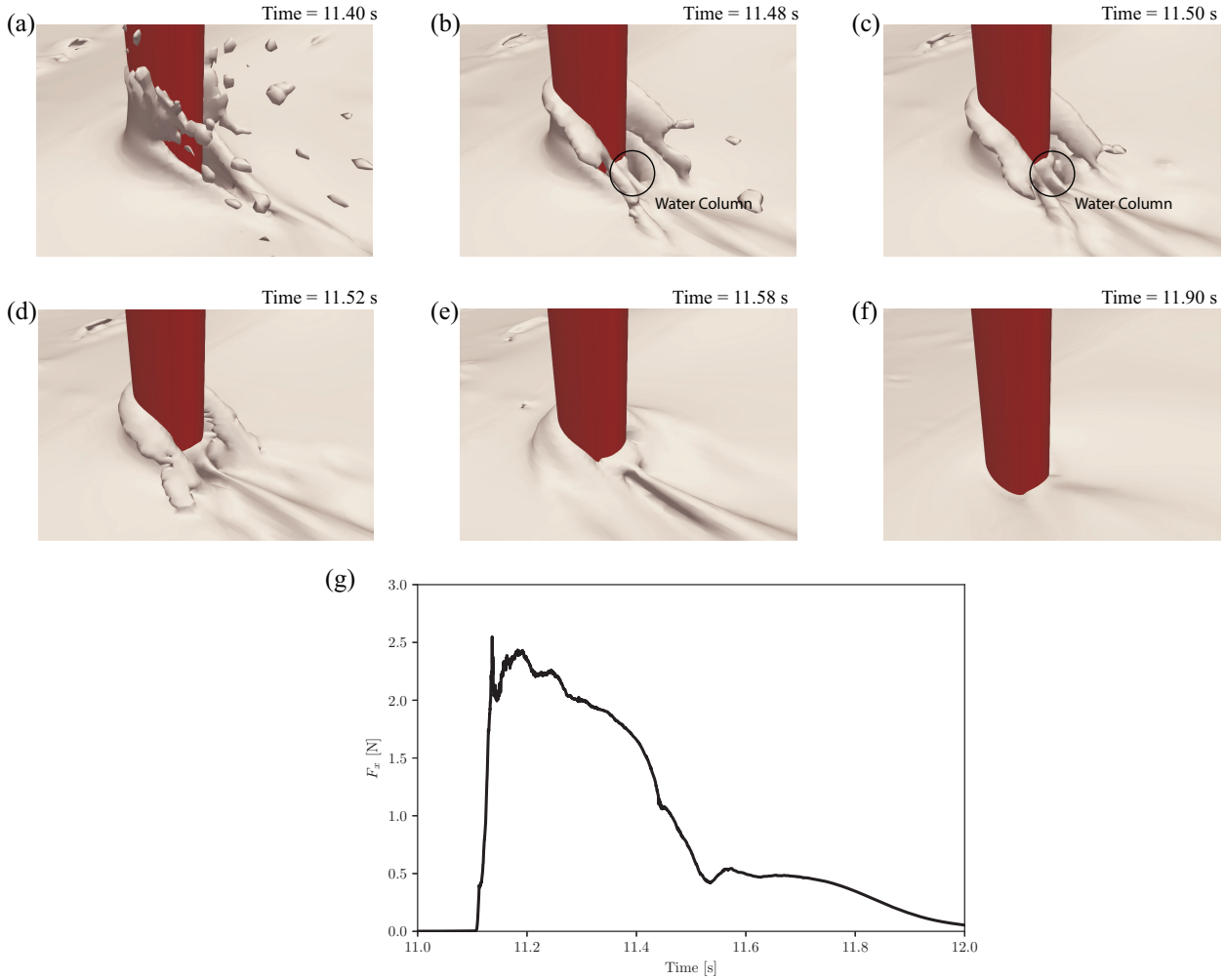

Figure 15: (a-f) Snapshots of the free surface near the cylinder around the time when secondary load cycle occurs: (a) at the time of the overtopping flow passing the front side of the cylinder, (b) at the time when the water column starts to build, (c) at the time during the water column grows, (d) at the time when the water column reaches its maximum and starts to fall down, (e) at the time when the water column is collapsing, (f) at the end of the secondary load cycle. The results are from the plunging-breaker case. The incident wave condition is $H = 0.20$ m, $R_c = 0.15$ m and $T = 2$ s. (g) The corresponding time series of the inline force on the cylinder.

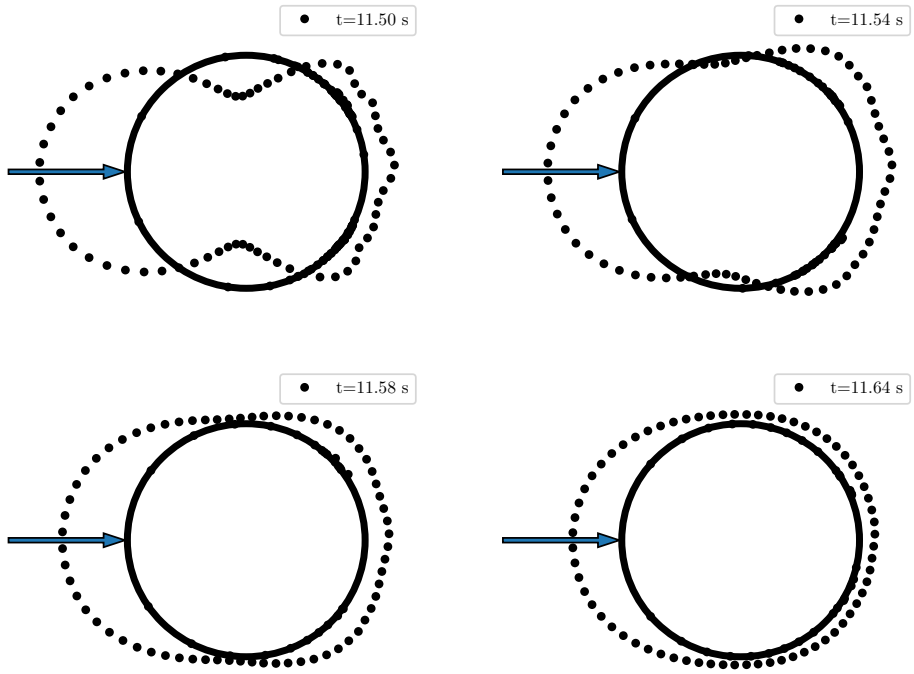

Figure 16: Distribution of the pressure integration in the circumference direction around the time when the secondary load cycle occurs. The pressure is integrated in the same way as shown in Fig. 14. The results are from the plunging-breaker case. The incident wave condition is $H = 0.20$ m, $R_c = 0.15$ m and $T = 2$ s.

each individual i-th wave cycle, the wave height H_i and wave period T_i can be determined, which is further used to obtain F_{0m} for each cycle.

Two sets of irregular wave tests were conducted in parallel, in order to obtain more data points. JONSWAP spectrum was used in both cases with significant wave height $H_s = 0.8$ m and 1 m, respectively. In both cases, the peak period $T_p = 6$ s, the enhancement factor $\gamma = 3.3$ and the freeboard $R_c = H_s$. For each test, a duration of 160 s (about 30 waves) simulation could be completed with 24 cores within 2 weeks. Fig. 18 shows the time series of surface elevation near the wave inlet and the inline force due to overtopping flow for the case with $H_s = 0.8$ m. The effect of wave irregularity on overtopping is primarily on the breaking process. The run-down of overtopping flow on the seawall slope will interfere the breaking of the next wave, so a wave in an irregular wave train may not break in the same way when it is in a regular wave train. This effect, however, is found to be insignificant for the prediction of the maximum inline force. As shown in Fig. 17, the relative difference between the directly simulated (F_s) maximum inline force and the estimate (F_p) using the empirical predictor is generally within 30%, which is in agreement of the accuracy of the predictor shown in the right figure of Fig. 18. This suggests that the force predictor can indeed be used in real applications via a wave-by-wave approach.

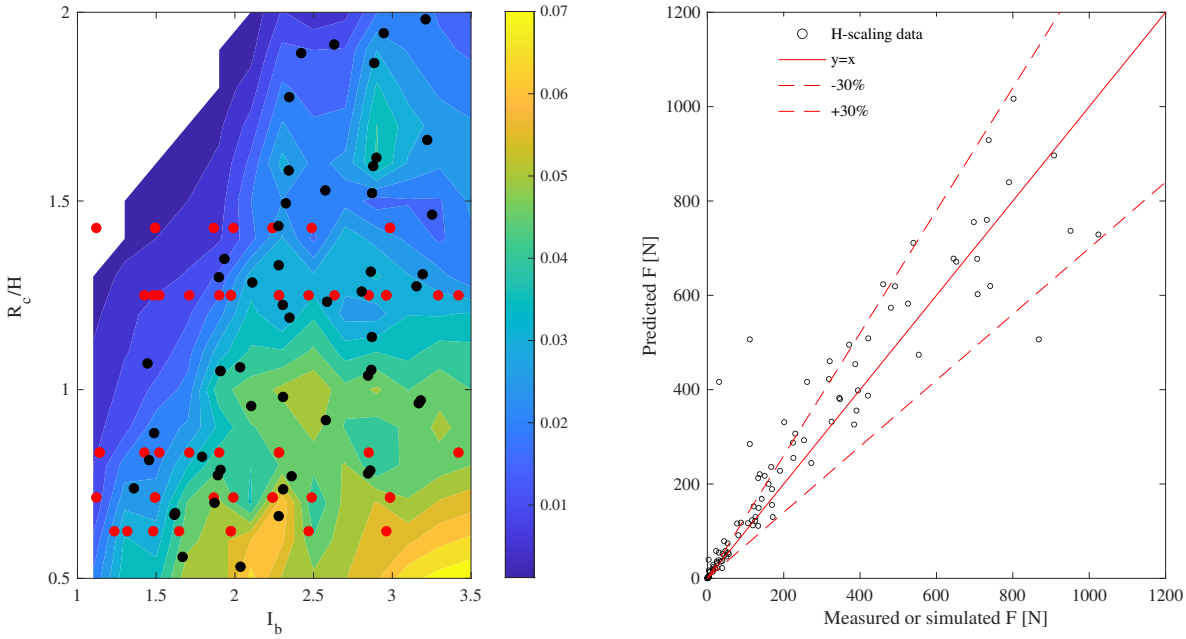

Figure 17: Left: The scaling parameter C_H as a function of R_c/H and I_b. The red dots are the simulated results in prototype scale and the black dots are the experimental results in model scale. Right: Comparison between the measured (or directly simulated) maximum inline force and the estimates using the empirical predictor (Eq. (9)) and the calibrated scaling parameter in the left panel.

6. Summary and conclusions

The interaction of overtopping flow with a cylinder as a surrogate of human body is numerically investigated in the present paper, where a VOF based RANS model with $k-\omega$ SST turbulence closure model is utilised. With a reasonable resolution of about 3 million cells, the model can properly resolve wave propagation, breaking on the slope, overtopping and the 3-dimensional interaction between the overtopping flow and the cylinder. Validation tests against experimental data were carried out for both plunging-breaker and surging-breaker cases. The plunging-breaker tends to produce a thin layer of aerated flow with fast speed, while the surging-breaker gives a thicker and much less aerated overtopping flow. It is found that the model is capable to capture the general shape and the peaks of the overtopping flow depth and the inline force, although the high-frequency oscillations due to entrained air are not captured for the plunging-breaker case.

While for the surging-breaker case, the inline force is dominated by the main peak, time series of the inline force for the plunging-breaker case suggests that during one overtopping event, there can be a first impact peak, a main peak and a secondary peak. The first impact peak is generated when the tip of the overtopping flow slams onto the cylinder, and is strongly associated with the local flow at the tip. There is a strong cycle-to-cycle variation as the tip flow is not exactly repetitive. The main peak occurs after the

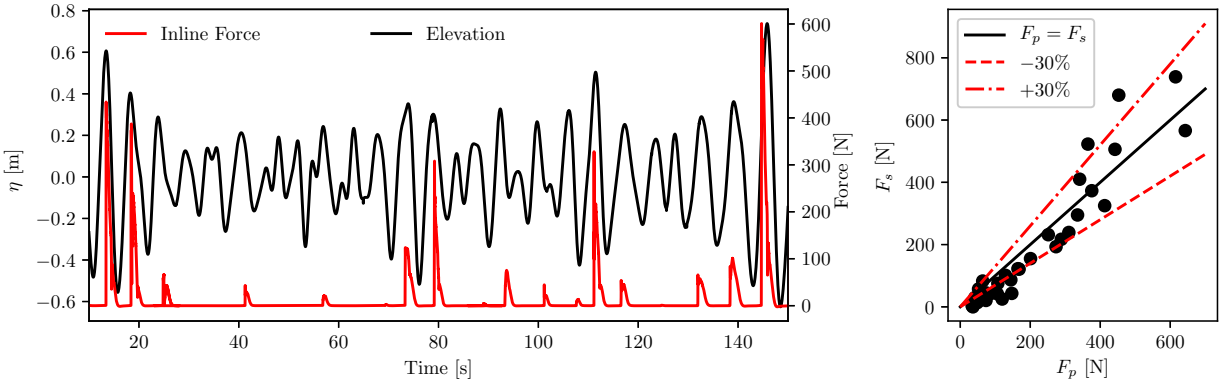

Figure 18: Left: Comparison of the time series of the surface elevation near the inlet of the wave tank and the induced inline force on the cylinder due to the overtopping flow under irregular wave conditions. The time series have been aligned to enable a wave-to-wave analysis. The incident irregular wave condition is based on the JONSWAP spectrum with a significant wave height H_s of 0.8 m, peak period T_p of 6 s and freeboard R_c of 1 m. Right: Comparison between the predicted force F_p using the derived formula in Eq. (9) and the simulated force F_s from both cases with irregular wave conditions.

first impact peak, and is dominated by the inertia effects. By extracting the pressure distribution around the cylinder when the main peak occurs, it is found that the peak is driven by the asymmetric distribution in the front and back side of the cylinder. The secondary cycle is associated with the complex flow behind the cylinder. A water column at the back side of the column is built due to the returned flow, and the secondary peak is produced by the collapsing of this water column.

The validated numerical wave flume was used to generate overtopping flows that could not be obtained in the experiments in Part I. Namely, a large sets of simulations for seawalls with different slopes (1:2, 1:3 and 1:4) were conducted to collect data of the maximum inline force (the main peak) on the cylinder. By combining physical and numerical simulations, a large dataset was developed for calibrating a simple predictor for the maximum inline force. Finally, a numerical experiment involving irregular incident waves was conducted to demonstrate that the simple predictor can be used for real application in a wave-by-wave approach.

The two companion papers combine experimental and numerical modelling to investigate the wave overtopping on a sloped seawall and its interaction with a cylinder. The experiments provide direct observations of the overall physical process, as well as the measurements of some key physical quantities (e.g., the inline force). The validated numerical model provides comprehensive information on the overtopping flow velocity and the pressure distribution around the cylinder, which cannot be measured in the experiments. Moreover, the numerical model was applied to expand the dataset for calibrating empirical formula. In recent years, high-fidelity numerical modelling is becoming tangible because of the fast advancement of supercomputing resources and open-source codes. We believe that numerical modelling will have more weightage in the

future coastal-engineering research, and such a combined numerical and experimental research will become more popular. This study is limited to wave overtopping at a sloped (and impermeable) seawall with a deep foreshore, which is motivated by the revetments protecting the reclaimed land in Singapore. This is only a small piece of the entire overtopping framework, so future work is needed to cover more topographic and flow conditions, e.g., seawalls with a shallow foreshore, porous structure, seawalls with berms, obliquely incident waves and etc.

Acknowledgement

This work was supported by the Climate Resilience Study Funds (CRSF) through Building and Construction Authority (BCA) and Public Utilities Board (PUB) of Singapore. The Department of Civil and Environmental Engineering in National University of Singapore is acknowledged for allowing us to use the hydraulic laboratory. National Supercomputing Centre Singapore (NSCC) is acknowledged for providing the high-performance computing facilities for the present study.

References

Allsop W, Bruce T, Pearson J, Alderson J, Pullen T. Violent wave overtopping at the coast, when are we safe? In: International Conference on Coastal Management 2003. Thomas Telford Publishing; 2003. p. 54–69.

Altomare C, Suzuki T, Chen X, Verwaest T, Kortenhaus A. Wave overtopping of sea dikes with very shallow foreshores. Coastal Engineering 2016;116:236–57. doi:10.1016/j.coastaleng.2016.07.002.

Bakhtyar R, Barry DA, Yeganeh-Bakhtiary A, Ghaheri A. Numerical simulation of surf–swash zone motions and turbulent flow. Advances in Water Resources 2009;32(2):250–63.

Bosman G, Van Der Meer J, Hoffmans G, Schüttrumpf H, Verhagen HJ. Individual overtopping events at dikes. In: Coastal Engineering 2008: (In 5 Volumes). World Scientific; 2009. p. 2944–56.

Brackbill JU, Kothe DB, Zemach C. A continuum method for modeling surface tension. Journal of computational physics 1992;100(2):335–54.

Bradford SF. Numerical simulation of surf zone dynamics. Journal of Waterway, Port, Coastal, and Ocean Engineering 2000;126(1):1–13.

Cao D, Yuan J, Chen H, Zhao K, Liu PLF. Wave overtopping flow striking a cylinder on the crest of a sloped seawall. part i: An experimental study; 2020. Unpublished.

Chella MA, Bihs H, Myrhaug D, Muskulus M. Hydrodynamic characteristics and geometric properties of plunging and spilling breakers over impermeable slopes. Ocean Modelling 2016;103:53–72.

Chen X, Hofland B, Altomare C, Suzuki T, Uijttewaal W. Forces on a vertical wall on a dike crest due to overtopping flow. Coastal Engineering 2015;95:94–104. doi:10.1016/j.coastaleng.2014.10.002.

Chen X, Hofland B, Uijttewaal W. Maximum overtopping forces on a dike-mounted wall with a shallow foreshore. Coastal Engineering 2016;116:89–102. URL: http://dx.doi.org/10.1016/j.coastaleng.2016.06.004. doi:10.1016/j.coastaleng.2016.06.004.

Chuang WL, Chang KA, Mercier R. Green water velocity due to breaking wave impingement on a tension leg platform. Experiments in Fluids 2015;56(7):139.

Chuang WL, Chang KA, Mercier R. Kinematics and dynamics of green water on a fixed platform in a large wave basin in focusing wave and random wave conditions. Experiments in Fluids 2018;59(6):100.

De Finis S, Romano A, Bellotti G. Numerical and laboratory analysis of post-overtopping wave impacts on a storm wall for a dike-promenade structure. Coastal Engineering 2020;155:103598.

De Rouck J, Van Doorslaer K, Versluys T, Ramachandran K, Schimmels S, Kudella M, Trouw K. Full scale impact tests of an overtopping bore on a vertical wall in the large wave flume (gwk) in hannover. Coastal Engineering Proceedings 2012;1(33):structures–62.

EurOtop . Manual on wave overtopping of sea defences and related structures. an overtopping manual largely based on european research, but for worldwide application. Van der Meer, J W and Allsop, N W H and Bruce, T and De Rouck, J and Kortenhaus, A and Pullen, T and Schüttrumpf, H and Troch, P and Zanuttigh, B 2018;.

Ghadirian A, Bredmose H. Detailed force modelling of the secondary load cycle. Journal of Fluid Mechanics 2020;889:A21. URL: https://www.cambridge.org/core/product/identifier/S0022112020000701/type/journal{_}article. doi:10.1017/jfm.2020.70.

Hirt CW, Nichols BD. Volume of fluid (vof) method for the dynamics of free boundaries. Journal of computational physics 1981;39(1):201–25.

Hsiao SC, Lin TC. Tsunami-like solitary waves impinging and overtopping an impermeable seawall: Experiment and rans modeling. Coastal Engineering 2010;57(1):1–18.

Hu K, Mingham CG, Causon DM. Numerical simulation of wave overtopping of coastal structures using the non-linear shallow water equations. Coastal engineering 2000;41(4):433–65.

Jacobsen NG, Fuhrman DR, Fredsøe J. A wave generation toolbox for the open-source CFD library: OpenFoam®. International Journal for Numerical Methods in Fluids 2012;70(9):1073–88. doi:10.1002/fld.2726.

Jonkman S, Penning-Rowsell E. Human instability in flood flows 1. JAWRA Journal of the American Water Resources Association 2008;44(5):1208–18.

Kihara N, Niida Y, Takabatake D, Kaida H, Shibayama A, Miyagawa Y. Large-scale experiments on tsunami-induced pressure on a vertical tide wall. Coastal engineering 2015;99:46–63.

Lin P, Liu PLF. A numerical study of breaking waves in the surf zone. Journal of fluid mechanics 1998;359:239–64.

Losada IJ, Lara JL, Guanche R, Gonzalez-Ondina JM. Numerical analysis of wave overtopping of rubble mound breakwaters. Coastal engineering 2008;55(1):47–62.

Mares-Nasarre P, Argente G, Gómez-Martín ME, Medina JR. Overtopping layer thickness and overtopping flow velocity on mound breakwaters. Coastal Engineering 2019;154(September). doi:10.1016/j.coastaleng.2019.103561.

Martínez-Gomariz E, Gómez M, Russo B. Experimental study of the stability of pedestrians exposed to urban pluvial flooding. Natural hazards 2016;82(2):1259–78.

Van der Meer J, Bruce T. New Physical Insights and Design Formulas on Wave Overtopping at Sloping and Vertical Structures. Journal of Waterway, Port, Coastal, and Ocean Engineering 2013;140(6):04014025. doi:10.1061/(asce)ww.1943-5460.0000221.

Van der Meer JW, Verhaeghe H, Steendam GJ. The new wave overtopping database for coastal structures. Coastal Engineering 2009;56(2):108–20. URL: http://dx.doi.org/10.1016/j.coastaleng.2008.03.012. doi:10.1016/j.coastaleng.2008.03.012.

Molines J, Herrera MP, Gómez-Martín ME, Medina JR. Distribution of individual wave overtopping volumes on mound breakwaters. Coastal Engineering 2019;149(December 2018):15–27. URL: https://doi.org/10.1016/j.coastaleng.2019.03.006. doi:10.1016/j.coastaleng.2019.03.006.

Paulsen BT, Bredmose H, Bingham HB, Jacobsen NG. Forcing of a bottom-mounted circular cylinder by steep regular water waves at finite depth. Journal of Fluid Mechanics 2014;755:1–34. doi:10.1017/jfm.2014.386.

Pullen T, Allsop W, Bruce T, Pearson J. Field and laboratory measurements of mean overtopping discharges and spatial distributions at vertical seawalls. Coastal Engineering 2009;56(2):121–40. URL: http://dx.doi.org/10.1016/j.coastaleng.2008.03.011. doi:10.1016/j.coastaleng.2008.03.011.

Riise BH, Grue J, Jensen A, Johannessen TB. A note on the secondary load cycle for a monopile in irregular deep water waves. Journal of Fluid Mechanics 2018;849.

Roenby J, Bredmose H, Jasak H. A computational method for sharp interface advection. Royal Society Open Science 2016;3(11). doi:10.1098/rsos.160405.

Romano A, Bellotti G, Briganti R, Franco L. Uncertainties in the physical modelling of the wave overtopping over a rubble mound breakwater: The role of the seeding number and of the test duration. Coastal Engineering 2015;103:15–21. URL: http://dx.doi.org/10.1016/j.coastaleng.2015.05.005. doi:10.1016/j.coastaleng.2015.05.005.

Russo B, Gómez M, Macchione F. Pedestrian hazard criteria for flooded urban areas. Natural hazards 2013;69(1):251–65.

Ryu Y, Chang KA. Green water void fraction due to breaking wave impinging and overtopping. Experiments in Fluids 2008;45(5):883–98. doi:10.1007/s00348-008-0507-3.

Ryu Y, Chang KA, Mercier R. Runup and green water velocities due to breaking wave impinging and overtopping. Experiments in Fluids 2007;43(4):555–67. doi:10.1007/s00348-007-0332-0.

Schüttrumpf H, Oumeraci H. Layer thicknesses and velocities of wave overtopping flow at seadikes. Coastal Engineering 2005;52(6):473–95. doi:10.1016/j.coastaleng.2005.02.002.

Shafiei S, Melville BW, Shamseldin AY. Experimental investigation of tsunami bore impact force and pressure on a square prism. Coastal Engineering 2016;110:1–16. doi:10.1016/j.coastaleng.2015.12.006.

Stansby PK, Feng T. Surf zone wave overtopping a trapezoidal structure: 1-d modelling and piv comparison. Coastal Engineering 2004;51(5-6):483–500.

Van Bergeijk V, Warmink J, van Gent M, Hulscher S. An analytical model of wave overtopping flow velocities on dike crests and landward slopes. Coastal Engineering 2019;149(March):28–38. doi:10.1016/j.coastaleng.2019.03.001.

Van Doorslaer K, Romano A, De Rouck J, Kortenhaus A. Impacts on a storm wall caused by non-breaking waves overtopping a smooth dike slope. Coastal Engineering 2017;120(December 2016):93–111. URL: http://dx.doi.org/10.1016/j.coastaleng.2016.11.010. doi:10.1016/j.coastaleng.2016.11.010.

Wang Z, Zou Q, Reeve D. Simulation of spilling breaking waves using a two phase flow cfd model. Computers & Fluids 2009;38(10):1995–2005.

Xie Z. Two-phase flow modelling of spilling and plunging breaking waves. Applied Mathematical Modelling 2013;37(6):3698–713. URL: http://dx.doi.org/10.1016/j.apm.2012.07.057. doi:10.1016/j.apm.2012.07.057.

Yeh H. Maximum Fluid Forces in the Tsunami Runup Zone. Journal of Waterway, Port, Coastal, and Ocean Engineering 2006;132(6):496–500. URL: http://www.worldscientific.com/doi/abs/10.1142/9789812774613{_}0018http://ascelibrary.org/doi/10.1061/{%}28ASCE{%}290733-950X{%}282006{%}29132{%}3A6{%}28496{%}29. doi:10.1061/(ASCE)0733-950X(2006)132:6(496).